This article was downloaded by: [North Carolina State University]
On: 08 October 2012, At: 13:35
Publisher: Taylor & Francis
Informa Ltd Registered in England and Wales Registered Number: 1072954 Registered office: Mortimer House, 37-41 Mortimer Street, London W1T 3JH, UK

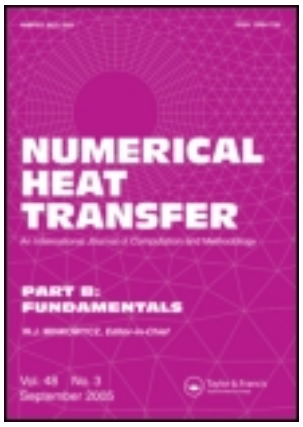

Numerical Heat Transfer, Part B: Fundamentals: An International Journal of Computation and Methodology
Publication details, including instructions for authors and subscription information:
http://www.tandfonline.com/loi/unhb20

COMPUTATION OF RADIANT HEAT TRANSFER ON A NONORTHOGONAL MESH USING THE FINITE-VOLUME METHOD

E. H. Chui [a] & G. D. Raithby [a]
[a] Department of Mechanical Engineering, University of Waterloo, Waterloo, Canada N2L, 3G1, Canada

Version of record first published: 23 Mar 2007.

To cite this article: E. H. Chui & G. D. Raithby (1993): COMPUTATION OF RADIANT HEAT TRANSFER ON A NONORTHOGONAL MESH USING THE FINITE-VOLUME METHOD, Numerical Heat Transfer, Part B: Fundamentals: An International Journal of Computation and Methodology, 23:3, 269-288

To link to this article: http://dx.doi.org/10.1080/10407799308914901

PLEASE SCROLL DOWN FOR ARTICLE

Full terms and conditions of use: http://www.tandfonline.com/page/terms-and-conditions

This article may be used for research, teaching, and private study purposes. Any substantial or systematic reproduction, redistribution, reselling, loan, sub-licensing, systematic supply, or distribution in any form to anyone is expressly forbidden.

The publisher does not give any warranty express or implied or make any representation that the contents will be complete or accurate or up to date. The accuracy of any instructions, formulae, and drug doses should be independently verified with primary sources. The publisher shall not be liable for any loss, actions, claims, proceedings, demand, or costs or damages whatsoever or howsoever caused arising directly or indirectly in connection with or arising out of the use of this material.

Numerical Heat Transfer, Part B, vol. 23, pp. 269-288, 1993

COMPUTATION OF RADIANT HEAT TRANSFER ON A NONORTHOGONAL MESH USING THE FINITE-VOLUME METHOD

E. H. Chui and G. D. Raithby
Department of Mechanical Engineering, University of Waterloo, Waterloo, Canada, Canada N2L 3G1

The finite-volume method has been shown to effectively predict radiant exchange in geometrically simple enclosures where the medium is gray, absorbing, emitting, and scattering. Cartesian and circular cylindrical meshes have always been used. The present article shows that the method applies equally well to geometrically complex enclosures where nonorthogonal, boundary-fitted meshes are used. This development permits radiant heat transfer to be computed on the same mesh employed to solve the equations of fluid motion.

Downloaded by [North Carolina State University] at 13:35 08 October 2012

INTRODUCTION

To predict the fluid flow and convective heat transfer in the geometrically complex systems of practical interest, computational methods are normally implemented on nonorthogonal, boundary-fitted meshes. Many such problems also require prediction of the radiant heat transfer, where the medium affects the heat transfer through emission, absorption, and scattering. The radiative transfer equation (or RTE) governs this radiant exchange. Although it is desirable to solve this equation on the same computational mesh used for the fluid flow, there has been very little discussion in the literature on solution methods that use nonorthogonal meshes (see reviews by Howell [1] and Viskanta and Mengüç [2]). The spherical harmonics method of Mengüç and Viskanta [3, 4]), the discrete ordinates method of Fiveland [5], the zonal method of Larsen and Howell [6], the six flux method of Siddall and Selçuk [7], and the discrete transfer method of Lockwood and Shah [8] are all presented using rectangular or cylindrical meshes.

The finite-volume method (FVM), developed by the present authors, has also been applied only on Cartesian [9] and cylindrical [10] meshes. The goal of this article is to demonstrate the application of this method on nonorthogonal, quadrilateral element meshes.

This work was supported by a contract from the Combustion and Carbonization Research Laboratory, CANMET, of the Energy Mines and Resources Department of the Canadian Federal Government, under the scientific authority of P. Hughes. The authors are also grateful for the additional financial assistance received from the Natural Science and Engineering Research Council of Canada.

Copyright © 1993 Taylor & Francis
1040-7790/93 $10.00 + .00

NOMENCLATURE

A_f	area of surface panel f, m^2	δ	Kronecker delta function
I	radiant intensity, $W/(m^2\ sr)$	ϵ	emissivity
$\bar{I}^l$	inscattering intensity, Eqs. (2) and (7)	θ	polar angle measured from z axis
I_b	blackbody intensity, $\sigma T^4/\pi$	κ	extinction coefficient, $K_a + \sigma_s$, 1/m
I_β	intensity at boundary	σ	Stefan-Boltzmann constant
I^l_{if}	intensity at integration point if within ω^l	σ_s	scattering coefficient, 1/m
I^l_P	intensity at node P within ω^l	ϕ	azimuthal angle measured from x axis in x-y plane
I^l_{uf}	upstream intensity for integration point on surface panel f within ω^l	Φ	scattering phase function, Eq. (2)
K_a	absorption coefficient, 1/m	$\bar{\Phi}$	new variable for phase function, Eq. (8)
N_x, N_y	number of control volumes in the x and y directions	ψ	scattering angle, between s and s′ in Eq. (2)
N_θ, N_ϕ	number of control volumes in the polar (θ) and azimuthal (ϕ) directions	ω_s	scattering albedo, $\sigma_s/(\sigma_s + K_a)$
		ω	solid angle, sr
n	unit normal to a surface of control volume		
q	radiant heat flux, W/m^2	**Subscripts and Superscripts**	
Q^l_f	radiant energy within ω^l crossing surface panel f, W	b	refers to blackbody
r	position vector	f	refers to panel f on the surface of a control volume
R^l	intensity source function within ω^l, Eq. (6)	if	refers to the integration point on surface panel f
s	distance in direction of s, m	l	associated with discrete solid angle ω^l
s	unit vector in direction of intensity	nb	refers to neighboring volumes
S	path length, m	N, S, E, W	north, south, east, west
T	temperature, K	NW, NE, SW, SE	northwest, northeast, southwest, southeast
V	volume, m^3	P	refers to nodal point P
w_n	weight on node n within a quadrilateral element based on bilinear approximation, Eq. (9)	uf	interpolation location for intensity upstream of point if
x, y, z	Cartesian coordinates	w	enclosure wall
β, γ	local coordinates for a quadrilateral element, Fig. 2A		

Several features make the FVM attractive for the present purposes. The method was originally derived with nonorthogonal meshes in mind. It also guarantees global conservation of radiant energy, and captures the diffusion limit exactly for a strongly participating medium. The FVM has been shown to give accurate results for rectangular and cylindrical enclosures, anisotropic scattering is easy to treat, and rapid convergence can be achieved over a large range of optical thickness [11].

In the sections that follow, the discretization of the RTE on the nonorthogonal mesh is described, a new solution procedure is outlined, details related to special treatment at the boundaries are given, and the results of four test problems are presented. For simplicity, only two-dimensional problems are considered, and the medium is assumed to be gray.

Downloaded by [North Carolina State University] at 13:35 08 October 2012

RADIATIVE TRANSFER EQUATION

The transfer of radiant energy is governed by the radiative transfer equation (RTE) [12]:

$$\frac{dI(\mathbf{r}, \mathbf{s})}{ds} = -(K_a + \sigma_s)I(\mathbf{r}, \mathbf{s}) + K_a I_b(\mathbf{r}) + \sigma_s \bar{I}(\mathbf{r}, \mathbf{s}) \tag{1}$$

It describes the variation of radiant intensity $I(\mathbf{r}, \mathbf{s})$ at location $\mathbf{r}$ in direction $\mathbf{s}$. The four terms on the right side account for absorption, outscattering, emission, and inscattering, respectively. The inscattering term is defined by

$$\sigma_s \bar{I}(\mathbf{r}, \mathbf{s}) = \frac{\sigma_s}{4\pi} \int_{4\pi} I(\mathbf{r}, \mathbf{s}')\Phi(\mathbf{s}, \mathbf{s}')\, d\omega' \tag{2}$$

where $I(\mathbf{r}, \mathbf{s}')$ is the incident intensity from direction $\mathbf{s}'$ and Φ is the scattering phase function between $\mathbf{s}'$ and $\mathbf{s}$.

The principal goal here is to obtain a discrete representation of I both in space and direction using a finite-volume approach.

SPATIAL GRID

Figure 1A shows how an irregular geometry can be subdivided using a mesh made up of quadrilateral "elements." Each grid line intersection defines a node, denoted by a heavy dot. All dependent variables are stored at the nodes, and the equation for each variable is obtained from its discretized conservation equation for a volume surrounding the node. The volume associated with an interior node, such as P in Fig. 1A, is the sum of the four cross-hatched quadrants shown in Fig. 1B. The outside surfaces of the quadrants (the dashed lines) lie along lines that joint the midpoints of opposite sides of the element. The eight surface panels of the control volume are denoted by $f = 1, 2, \ldots, 8$. For panel f, if is the integration point lying at the center of the panel, A_f is its surface area, and $\mathbf{n}_f$ is the unit outward normal. For nodes adjacent to the boundary, such as P in Fig. 1C, the volume extends right to the physical boundary, and neighboring nodes lie on the boundary. For two-dimensional problems, the volume is assumed to have unit depth normal to the plane of Fig. 1. Except for minor details related to the volume adjacent to a surface, the grid system just described was proposed by Baliga and Patankar [13] and used to make fluid flow computations by Schneider and Raw [14].

ANGULAR DISCRETIZATION

The directional dependence of radiant intensity at every spatial node is captured by subdividing direction into discrete, nonoverlapping, solid angles of size ω^l. Total flexibility is allowed in choosing the individual size of ω^l provided $\Sigma\omega^l = 4\pi$. In practice, ω^l is defined by a range of polar angle θ and of azimuthal angle ϕ.

Downloaded by [North Carolina State University] at 13:35 08 October 2012

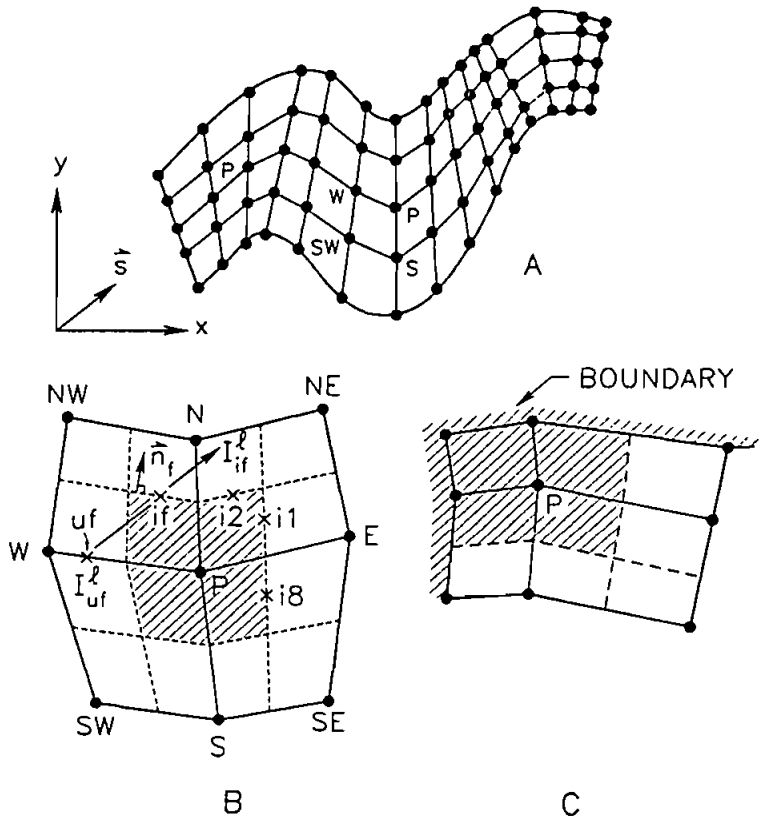

Fig. 1 (A) Sample computational mesh; (B) an interior control volume formed from assembly of four quadrants; (C) a control volume adjacent to the boundary.

FINITE-VOLUME APPROXIMATION

Implementing the FVM, the RTE [Eq. (1)] is integrated over control volume V_P and solid angle ω^l to yield the conservation constraint that the net radiant energy leaving through the surface of V_P within ω^l equals the net generation of radiant energy within V_P and ω^l by emission, absorption, and scattering. Approximating this generation term by nodal point values, the conservation balance becomes

$$\sum_{j=1}^{8} Q_f^l = [-(K_{a,P} + \sigma_{s,P})I_P^l + K_{a,P}I_{b,P} + \sigma_{s,P}\bar{I}_P^l]\omega^l V_P \tag{3}$$

where Q_f^l is the radiant energy within ω^l that crosses the surface panel f, I_P^l is the intensity within ω^l at node P, while $I_{b,P}$ and $\bar{I}_P^l$ are, respectively, the nodal blackbody intensity and the inscattering term. Defining I_{if}^l as the intensity at integration point if within ω^l,

Downloaded by [North Carolina State University] at 13:35 08 October 2012

$$Q_f^l \approx I_{if}^l A_f \int_{\omega^l} (\mathbf{s} \cdot \mathbf{n}_f)\, d\omega = I_{if}^l A_f D_f^l \tag{4}$$

where s is a unit vector in the direction of radiation and the integral D_f^l is evaluated analytically. Using a Taylor series expansion about integration *if*, Raithby and Chui [9] introduced the closure relation

$$I_{if}^l = I_{uf}^l e^{-\kappa_{if} S} + R_{if}^l (1 - e^{-\kappa_{if} S}) - \frac{1}{\kappa_{if}} \left(\frac{\partial R^l}{\partial s} \right)_{if} [1 - e^{-\kappa_{if} S}(1 + \kappa_{if} S)] \tag{5}$$

where I_{uf}^l is the intensity at point *uf* (see Fig. 1B) that lies distance S upstream from point *if*. $\kappa = K_a + \sigma_s$ is the extinction coefficient and variable R^l, defined in Eq. (6), embodies the emitting and scattering characteristics of the medium. The first term on the right side of Eq. (5) represents the remnant of intensity I_{uf}^l reaching *if*, while the last two terms incorporate the net change of intensity due to emission, absorption, and scattering from *uf* to *if*. Retention of the last term is crucial for the FVM to capture the optically thick limit.

The introduction of Eq. (5) generates three new unknowns: R_{if}^l, $(\partial R^l/\partial s)_{if}$ and I_{uf}^l. These must be related to nodal values before Eq. (3) can be solved. Attention is next turned to this matter.

Calculation of R_{if}^l and $(\partial R^l/\partial s)_{if}$

The variable R^l, is defined as

$$R^l = \frac{K_a I_b + \sigma_s \bar{I}^l}{\kappa} \tag{6}$$

where $I_b = (\sigma T^4/\pi)$ is the blackbody intensity and $\bar{I}^l$ is the inscattering term evaluated by approximating Eq. (2) with

$$\bar{I}^l = \frac{1}{4\pi} \sum_{l'}^{4\pi} I^{l'} \bar{\Phi} \tag{7}$$

where

$$\bar{\Phi} = \frac{\int_{\omega^l} \int_{\omega^{l'}} \Phi(l', l)\, d\omega^{l'}\, d\omega^l}{\omega^l} \tag{8}$$

the value of $\bar{\Phi}$ is obtained by exact or very accurate numerical integration of the phase function Φ. This formulation was discussed and tested by Chui et al. [10].

Since R^l is specified at nodal locations (such as nodes 1 to 4 in Fig. 2), R_{if}^l at integration points can be obtained by bilinear interpolation of nodal values; using the β, γ coordinate system shown in Fig. 2,

Downloaded by [North Carolina State University] at 13:35 08 October 2012

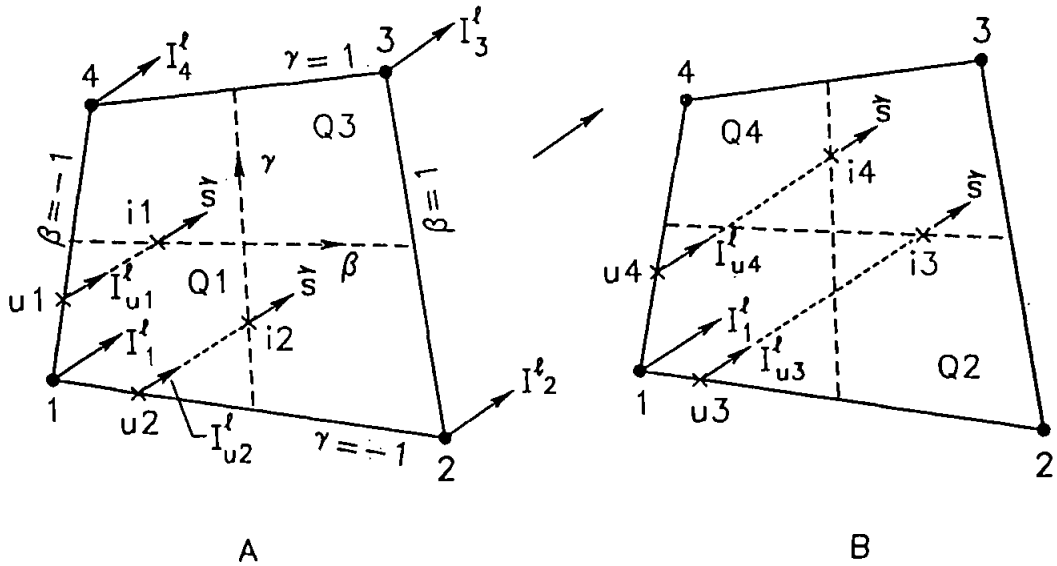

Fig. 2 Determination of integration point intensities on edges of quadrants Q1 to Q4.

$$R^l_{if} = R^l_1\frac{(1-\beta_{if})(1-\gamma_{if})}{4} + R^l_2\frac{(1+\beta_{if})(1-\gamma_{if})}{4} + R^l_3\frac{(1+\beta_{if})(1+\gamma_{if})}{4} + R^l_4\frac{(1-\beta_{if})(1+\gamma_{if})}{4}$$

or

$$R^l_{if} = \sum_{n=1}^{4} R^l_n w_n(\beta_{if}, \gamma_{if}) \tag{9}$$

where w_n is the bilinear interpolation weight on node n for the integration point if specified by the local coordinates $(\beta_{if}, \gamma_{if})$.

Differentiating Eq. (9), rewritten for general location (β, γ)

$$\left(\frac{\partial R^l}{\partial s}\right)_{if} = \sum_{n=1}^{4} R^l_n\left(\frac{\partial w_n}{\partial x}\frac{\partial x}{\partial s} + \frac{\partial w_n}{\partial y}\frac{\partial y}{\partial s}\right)_{\beta_{if},\gamma_{if}} \tag{10}$$

where $\partial x/\partial s$ and $\partial y/\partial s$ are direction cosines in direction s in the global x, y coordinate system.

For a given grid, w_n, $\partial w_n/\partial x$ and $\partial w_n/\partial y$ are calculated analytically once and stored. Equations (9) and (10) are then used when needed to determine R^l_{if}, $(\partial R^l/\partial s)_{if}$ at all integration points.

Downloaded by [North Carolina State University] at 13:35 08 October 2012

Calculation of I^l_{uf}

I^l_{uf} is the intensity at point uf upstream of integration point if. For example, points $u1$ and $u2$ associated with integration points $if = i1$ and $i2$, respectively, are shown in Fig. 2A. To find uf, the ray in the center of ω^l at point if is traced backward until it intersects with the surface of the element. I^l_{uf} can then be obtained by linear interpolation (e.g., I^l_{u1} can be obtained in terms of I^l_1 and I^l_4 in Fig. 2A). This practice leads to an equation for I^l_P that involves nodes downstream from node P; this complicates the solution of the equation, may lead to "wiggles" in the intensity, and reflects a physically incorrect influence. By slightly sacrificing accuracy, this downstream dependence can be avoided. For example, for quadrant $Q1$ in Fig. 2A and for the l direction shown, the following approximation is used: $I^l_{u1} = I^l_{u2} = I^l_1$. For $Q2$ in Fig. 2B, I^l_{u3} would be linearly interpolated from I^l_1 and I^l_2, as would I^l_{u4} from I^l_1 and I^l_4.

Algebraic Equation for I^l_P

With R^l_{if}, $(\partial R^l/\partial s)_{if}$ and I^l_{uf} defined, Eqs. (4) and (5) can be substituted into (3) to obtain an algebraic equation relating I^l_P to the intensities at neighboring nodes:

$$a^l_P I^l_P = \sum_{nb} a^l_{nb} I^l_{nb} + b^l_P \tag{11}$$

where the summation of nb is over the "upstream" neighbors. For the l direction shown in Fig. 1B, Eq. (11) takes the form

$$a^l_P I^l_P = a^l_W I^l_W + a^l_S I^l_S + a^l_{SW} I^l_{SW} + b^l_P \tag{12}$$

Equation (11) for each node together with boundary conditions provide the equation set for the nodal intensities in direction l. Similar equations are formed for other directions; the nodes that lie upstream of course change with l.

SOLUTION PROCEDURE

Overview

Provided scattering is not present, I^l_P in Eq. (11) is independent of downstream intensities. If the solver visits the nodes in the correct order, all terms on the right side of the equation will be known so I^l_P at each node can be found by direct substitution. This allows the solution to be obtained by moving from node to node in the optimal "marching order." For a Cartesian mesh it is immediately clear what the marching order must be, but for the irregular grid in Fig. 1A the order is no longer obvious.

To find a solution on irregular grids, there are two options. The equations could be solved by repeatedly sweeping across the grid until the convergence is achieved, without regard to the optimal order. Alternatively a "marching-order map" could be created that gives the optimal order in which the nodes should be visited. Once the angular discretization is fixed, a marching-order map can be constructed for each intensity direction, and this map can be stored for repeated use. Because the map is easy to generate, because it needs to be revised only when the spatial grid or angular discretization is

Downloaded by [North Carolina State University] at 13:35 08 October 2012

changed, and because it reduces solution costs, the creation of the map is the preferred alternative.

To obtain a preview of how a marching-order map might appear, the reader is referred to Fig. 4B. For the U-shaped region, the optimal order in which the nodes should be visited to solve for the intensity in the particular direction s is V1, V2, . . . , V15.

To create the map, the boundary elements are swept first to find the starting location. Once this is found, the entire marching sequence is derived by repeated application of a simple algorithm. Details are now provided.

Marching-Order Within an Element

The element shown in Fig. 2 contains four quadrants. Quadrant Q1 is part of the control volume for node 1, which requires the intensities I_{i1}^l and I_{i2}^l, which in turn require I_{u1}^l and I_{u2}^l. These and values of I_{u3}^l and I_{u4}^l are similarly required for the other control volumes associated with quadrants Q2, Q3, and Q4. According to the discretization scheme already described, $I_{u1}^l = I_{u2}^l = I_1^l$, so the equation for I_1^l is independent of I_4^l, I_2^l and I_3^l. Clearly, node 1 is farthest "upstream."

Similarly, the equation for I_4^l depends on I_1^l but not on I_2^l or I_3^l, and I_2^l depends on I_1^l but not on I_4^l or I_3^l. Therefore, nodes 2 or 4 are equally upstream, but not so far as node 1. Node 3 is least upstream.

The order in which the nodes in Fig. 2 should be visited is therefore 1–2or4–3, where 2or4 means the order may be 2–4 or 4–2. For a different direction s, the order may be different.

The general algorithm for node ordering within an element is shown in Fig. 3. Four sectors, denoted by φ_1 to φ_4, are defined by the quadrant boundaries. Once the sector, in which the intensity direction s falls, is determined, the table in Fig. 3 specifies the marching order. The special cases that arise for boundary elements are also shown. The stars denote locations where the intensity is known from boundary conditions.

Generation of the Marching-Order Map

The elements that make up the grid for a U-shaped region are shown in Fig. 4A. The node numbering is converted from the local numbering in Fig. 2 to a global numbering in Fig. 4 that uses (i, j), where i numbers the node along one set of grid lines and j along the other.

To find the starting location, the boundary elements are visited in any order until an interior node is found for which the only nodes farther upstream are boundary nodes that have known intensities from boundary conditions [e.g., in Fig. 4A, the intensities at nodes (1, 1), (2, 1), (3, 1), etc., are known from boundary conditions]. Applying the element algorithm in Fig. 3 to element $e1$ in Fig. 4A shows that node (3, 2) is farthest upstream among the unknown intensities in that element. But from element $e2$, node (2, 2) is farther upstream than (3, 2) and from $e3$, there is no unknown intensity that lies still farther upstream. Node (2, 2) is therefore a suitable starting location. This is denoted in Fig. 4B as V1.

With the farthest upstream node known, the map is generated by systematically finding which nodes are next farthest upstream. Applying the element algorithm to the elements that share the starting node (2, 2) shows that either (2, 3) or (3, 2) is next.

Downloaded by [North Carolina State University] at 13:35 08 October 2012

Downloaded by [North Carolina State University] at 13:35 08 October 2012

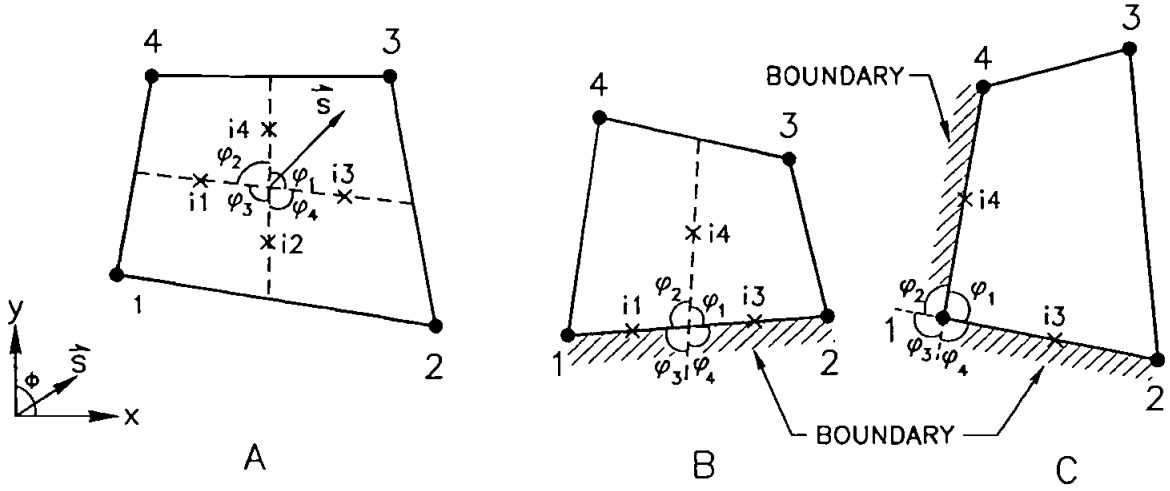

φ_1	1−2 OR 4−3	1*,2*−4−3	2*,4*−3
φ_2	2−1 OR 3−4	2*,1*−3−4	2*,1*−3−4
φ_3	3−2 OR 4−1	3−2−4−1	3−2 OR 4
φ_4	4−1 OR 3−2	4−1−3−2	4*,1*−3−2

Fig. 3 Variation of marching order with the sector φ in which a given intensity direction s lies. Superscript * denotes boundary intensities that are known.

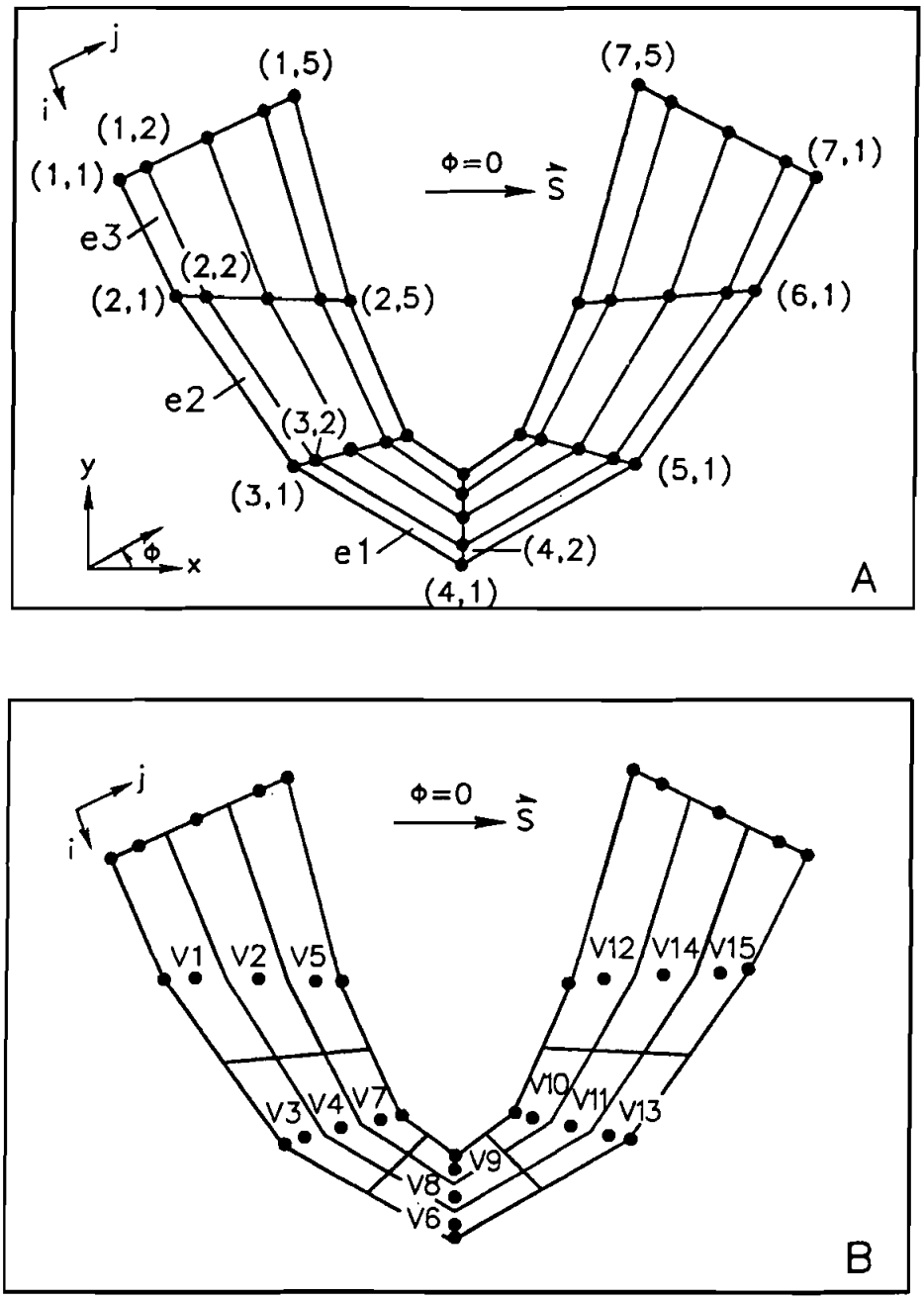

Fig. 4 (A) Determination of the starting location for a U-shaped domain in direction s; (B) map for the optimal marching order for the solver: V1, V2, . . . , V15.

Downloaded by [North Carolina State University] at 13:35 08 October 2012

These are therefore denoted by V2 and V3 in Fig. 4B. Repeated application of the algorithm to the elements that share these nodes reveals V4 and V5 in Fig. 4B are next, and so on until all interior nodes are numbered.

In special cases, where the grid is strongly kinked, the algorithm yields a conflict. To illustrate this conflict, node (4, 2) in Fig. 4A is shown enlarged in Fig. 5, where the neighboring elements are labeled $e1$ to $e4$. For $e1$, the marching order is (3, 2)-(3, 3)or(4, 2)-(4, 3); while for $e2$, it is (4, 3)-(4, 2)or(5, 3)-(5, 2). The order (4, 2)-(4, 3) for $e1$ is in conflict with (4, 3)-(4, 2) for $e2$. The conflict can be addressed by simultaneously solving the equations for all nodes that are in conflict. Alternatively, an order can be chosen arbitrarily, accepting the consequence that the marched solution will not be exactly correct from this point downstream. In practice, few conflicts arise, and iterations from the conflict point downstream yield rapid convergence.

BOUNDARY CONDITIONS

In this analysis, all boundaries are assumed diffuse-gray. For a surface at temperature T_B, the boundary condition for radiant intensity going into the medium at the surface nodes (see Fig. 1C) can be conveniently set as

$$I_B = \left[(1 - \epsilon_B)\sum_{l_{\text{in}}} Q_B^{l_{\text{in}}} + \epsilon_B A_B \sigma T_B^4\right]\frac{1}{\pi A_B} \tag{13}$$

The first term on the right side of Eq. (13) represent the reflected component where the summation of radiant flux Q [defined in Eq. (4)] is over all incoming l_{in} directions. The second term refers to the emissive component, which is proportional to the emissive power, σT_B^4, surface emissivity, ϵ_B, and area, A_B.

Special Considerations at the Boundary

For simple geometries, it is possible to subdivide direction such that the edge of a discrete solid angle (or "bundle") always lies tangent to the boundary. For complex geometries, the situation shown in Fig. 6 cannot be avoided; some rays in a bundle impinge on the surface from above (the "incoming" rays), while other rays in the same bundle originate from the surface (the "outgoing" rays). The incoming intensity will usually be very different from the outgoing intensity, and the approximation used in the model, that the intensity is uniform over each bundle, is unacceptable. New approximations are introduced for the bundles on the boundary where this situation is encountered.

The intensity associated with a discrete solid angle is assumed to be at the center of its bundle. For the case shown in Fig. 6A, therefore, the intensity over the incoming portion of the bundle is approximated by I^m; the intensity over the outgoing portion is approximated by I^{m+1}, the value of its immediate neighbor. For the bundle in Fig. 6B that straddles the boundary, the outgoing intensity is calculated from the boundary condition, while the incoming intensity is approximated by its immediate neighbor I^{m-1}. For the situation where I^m lies exactly along the surface, its value is not calculated at all, and both the incoming and outgoing intensities are approximated by their respective neighbor values.

Downloaded by [North Carolina State University] at 13:35 08 October 2012

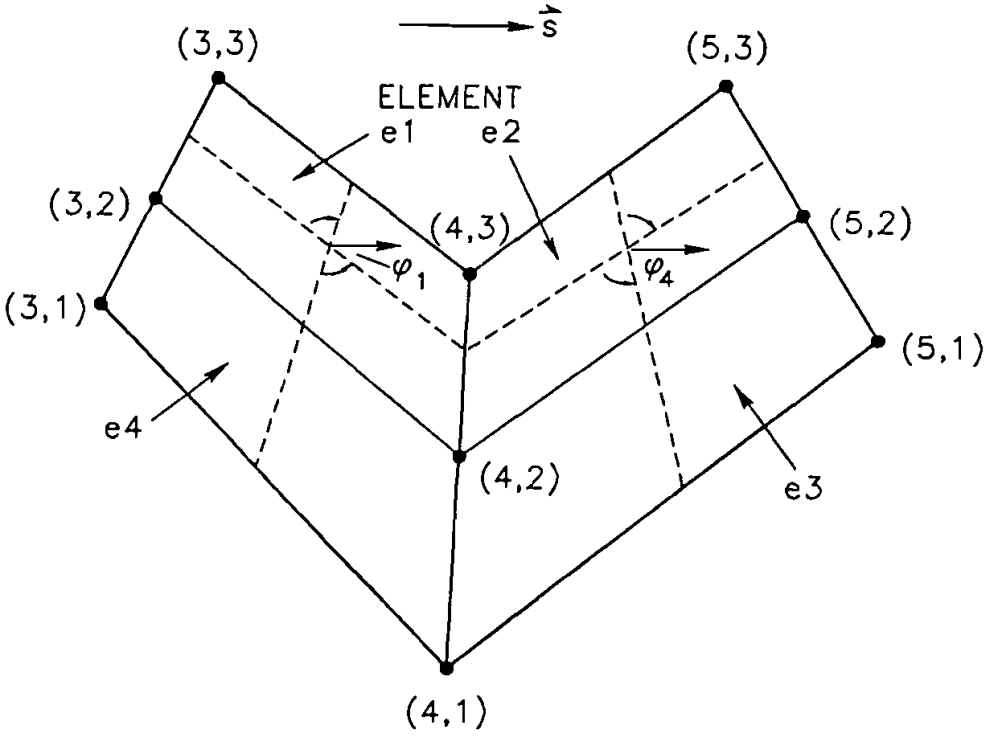

Fig. 5 Elements surrounding node (4, 2) in Fig. 4, where the marching-order algorithm encounters a conflict due to sharp grid turning.

These new approximations introduce new couplings between intensities of different directions at the bounding surface but they can be readily solved by iteration.

TEST RESULTS

The FVM just described is applicable to many two-dimensional radiation problems in very complex geometries. To demonstrate the method convincingly, however, it seems best to restrict attention to benchmark problems, and to problems where expected features of the solution can be checked.

Preliminary Tests

The nonorthogonal method was applied to calculate the radiant exchange in a square cavity with temperature-specified walls, and with an absorbing and isotropically scattering medium. The solution was compared to the earlier solution using a Cartesian code [9], and the results were found to be virtually the same. The increased generality of the nonorthogonal code increased the CPU time by a factor of 4.5 relative to the Cartesian code.

Downloaded by [North Carolina State University] at 13:35 08 October 2012

Downloaded by [North Carolina State University] at 13:35 08 October 2012

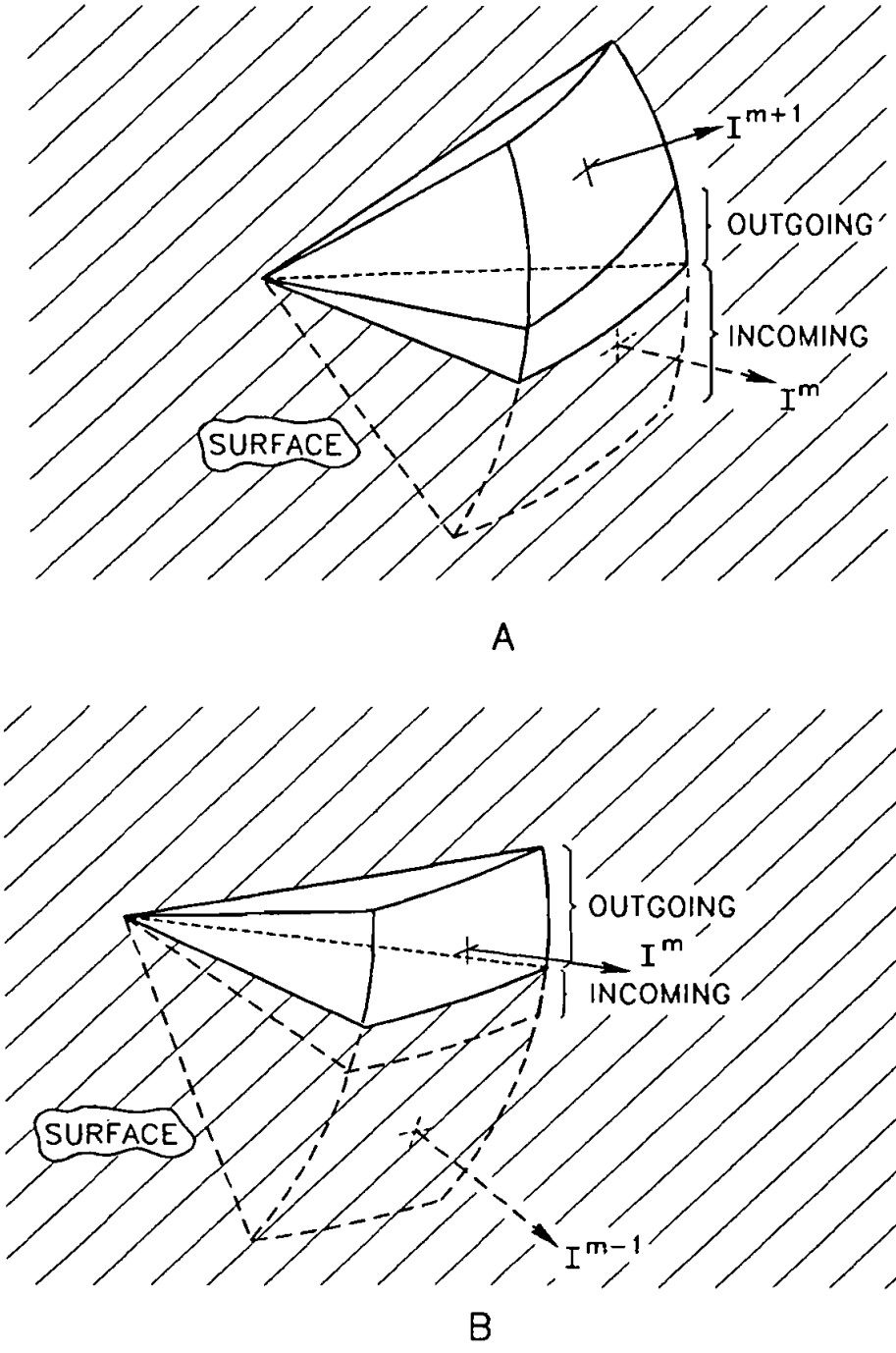

Fig. 6 Cases in which one discrete solid angle, or bundle, contains both incoming and outgoing radiation.

Infinite Concentric Cylinders

The second case is the prediction of radiative heat transfer in a long cylindrical annulus (see Fig. 7) containing a homogeneous, absorbing-emitting medium. The inner and outer radii of the annulus are 0.5 m and 1.0 m, respectively. The cylinder walls are assumed black and cold ($T_w = 0$), and the enclosed medium is held at a constant temperature of $T_g = 100$ K. The objective is to determine the heat flux in the radial direction.

A benchmark solution to the problem has been obtained by Dua and Cheng [15]. The dimensionless radial heat flux, $q_r^* = q_r/(\sigma T_4^4)$, is plotted in Fig. 7A for three different absorption coefficients: $K_a = 0.1$, 1.0, and 5.0 1/m. Errors of up to $\pm 5\%$ in these exact results are expected because they were obtained by digitizing published plots. Negative q_r^* indicates that the net radiative heat transfer is in the negative radial direction, toward the inner cylinder. Larger values of K_a result in larger q_r^* because emission is higher.

The elements that make up a coarse spatial grid are shown in Fig. 7B. The nodes are evenly spaced in the azimuthal and radial directions, except adjacent to the bound-

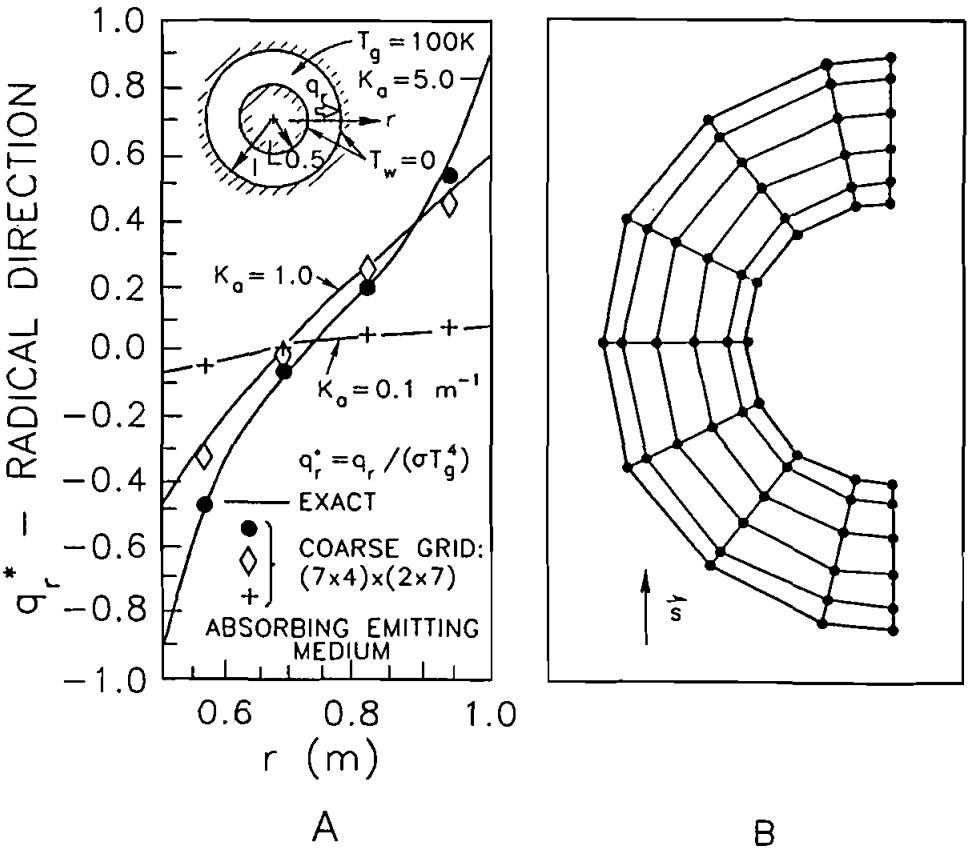

Fig. 7 (A) "Exact" results (see text) for the dimensionless radial heat flux and predictions on the coarse grid; (B) a coarse grid for a concentric annulus.

Downloaded by [North Carolina State University] at 13:35 08 October 2012

aries where the spacing is halved. As the azimuthal grid is refined, the polygon more closely approaches a circle.

One component of intensity was computed on the grid (see Fig. 7B) using the present nonorthogonal FVM; by the mapping procedure of Chui et al. [10], the spatial distribution of this component provides the complete axisymmetric intensity distribution. The resulting q_r^* values computed on the coarse grid shown in Fig. 7B ($N_x = 7$, $N_y = 4$, $N_\theta = 2$, where θ is the polar angle) are plotted in Fig. 7A.

The maximum discrepancy with the "exact" results was 15%, for the $K_a = 1.0$ case. As the grid was refined, the errors in the computed solution rapidly diminished to within the digitizing error. To obtain these solutions, iterations were required to account for the special considerations at the boundary stated earlier. The convergence criterion was that the q_r^* values should change less than 0.01% between iterations.

To obtain convergence on the coarse ($7 \times 4 \times 2$) mesh, 8 s of CPU time on a VAX 11-785 were needed. For the finest grid ($25 \times 16 \times 4$) used in this problem, 110 s were required. Preprocessing activity, including the calculation of geometric quantities and the marching-order map, took an additional 5 to 11 s.

Nonrectangular Enclosure

The last benchmark problem is to compute the net radiant flux, q_n, that falls on the north boundary of the nonrectangular enclosure shown in Fig. 8. The wall temperature was set to zero, and the medium temperature was set at $T_g = 100$ K. The medium was assumed to be nonscattering, and solutions were sought for absorption coefficients of $K_a = 0.1$, 1.0, and 10.0 1/m.

The exact solution to the radiative transfer equation at point (x, y) is

$$I(x, y, \theta, \phi) = I_b(1 - e^{-K_a S}) \tag{14}$$

where S is the distance from the point upstream to the enclosure wall along the ray defined by (θ, ϕ), and $I_b = \sigma T_g^4/\pi$. By computing the incident radiant intensities on the north wall of the enclosure, the "exact" local heat fluxes plotted in Fig. 8 were obtained. For $K_a = 10.0$, $q_n^* \sim 1.0$ along most of the wall, indicating that the transmission of radiation from the other enclosure walls has little effect except near the corners. Weak emission by the medium ($K_a = 0.1$) results in much lower heat transfer.

A nonorthogonal computational mesh was generated by locating an equal number of nodes on each boundary, uniformly spaced on each surface. The grid lines were generated by joining corresponding nodes on opposite sides of the enclosure by straight lines. The results from a $(N_x \times N_y) \times (N_\theta \times N_\phi) = (16 \times 16) \times (4 \times 16)$ grid are also plotted in Fig. 8; the maximum error was less than 1%. Results for other grids for $K_a = 0.1$ indicate that a fine discretization in the azimuthal direction (high N_ϕ) is needed to predict q_n^*, which is reasonable because the intensity distribution in nonuniform in this direction. For $K_a = 10.0$, good accuracy is obtained with a coarse directional mesh because the radiation falling on the surface has nearly uniform intensity; in this case, spatial refinement is of greater importance.

The numerical results in Fig. 8 required 200 CPU s on a VAX 11-785 for the finest grid, and an additional 30 s of preprocessing time. The coarse-grid solution required

Downloaded by [North Carolina State University] at 13:35 08 October 2012

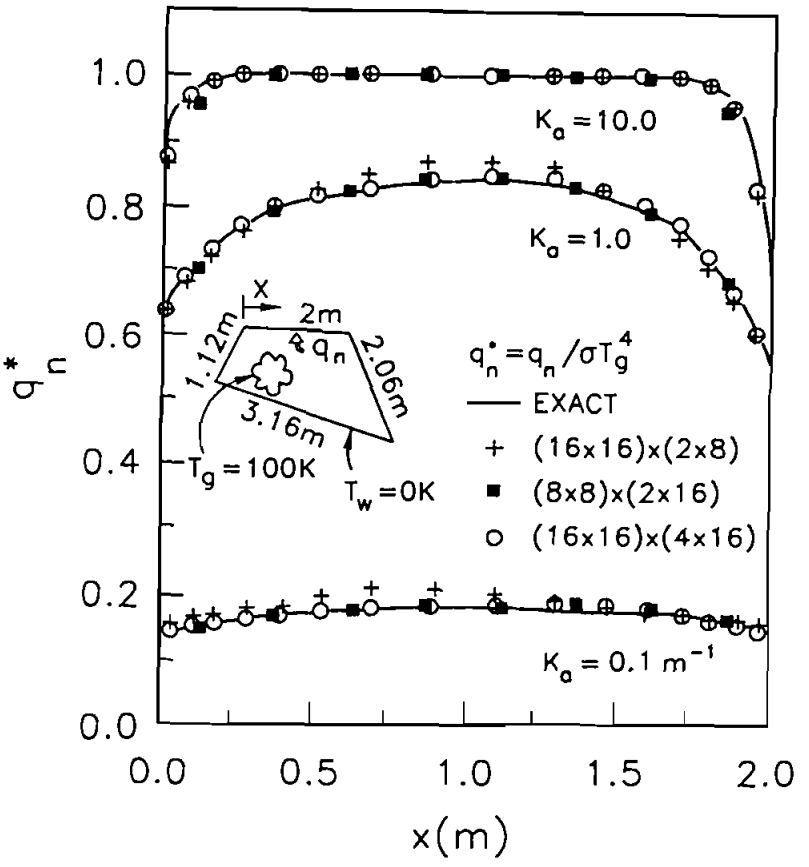

Fig. 8 Nondimensional radiant heat transfer on the north wall of the nonrectangular enclosure with an emitting gas at constant temperature T_g for absorption coefficients of K_a = 0.1, 1.0, 10.0 1/m.

about 24 s. Similar times were needed for nonzero wall temperatures, as reported in detail by Chui [16].

J-Shaped Enclosure

This test applies the FVM to a J-shaped domain (see Fig. 9), containing an absorbing, emitting, and anisotropically scattering medium. A uniform, diffuse radiant flux q_{in} was prescribed on the west wall, while the other walls were black and cold (T_w = 0 K). Radiative equilibrium was assumed. The absorption coefficient was K_a = 0.01, and the scattering coefficient was taken as σ_s = 1 except in the base case, where σ_s = 0 was used. The scattering-phase function was approximated by the delta-Eddington approximation [17],

$$\Phi(\psi) = 2f\delta(1 - \cos\psi) + (1 - f)(1 + 3g\cos\psi) \tag{15}$$

where ψ is the scattering angle. The f parameter governs the amount of forward scatter-

Downloaded by [North Carolina State University] at 13:35 08 October 2012

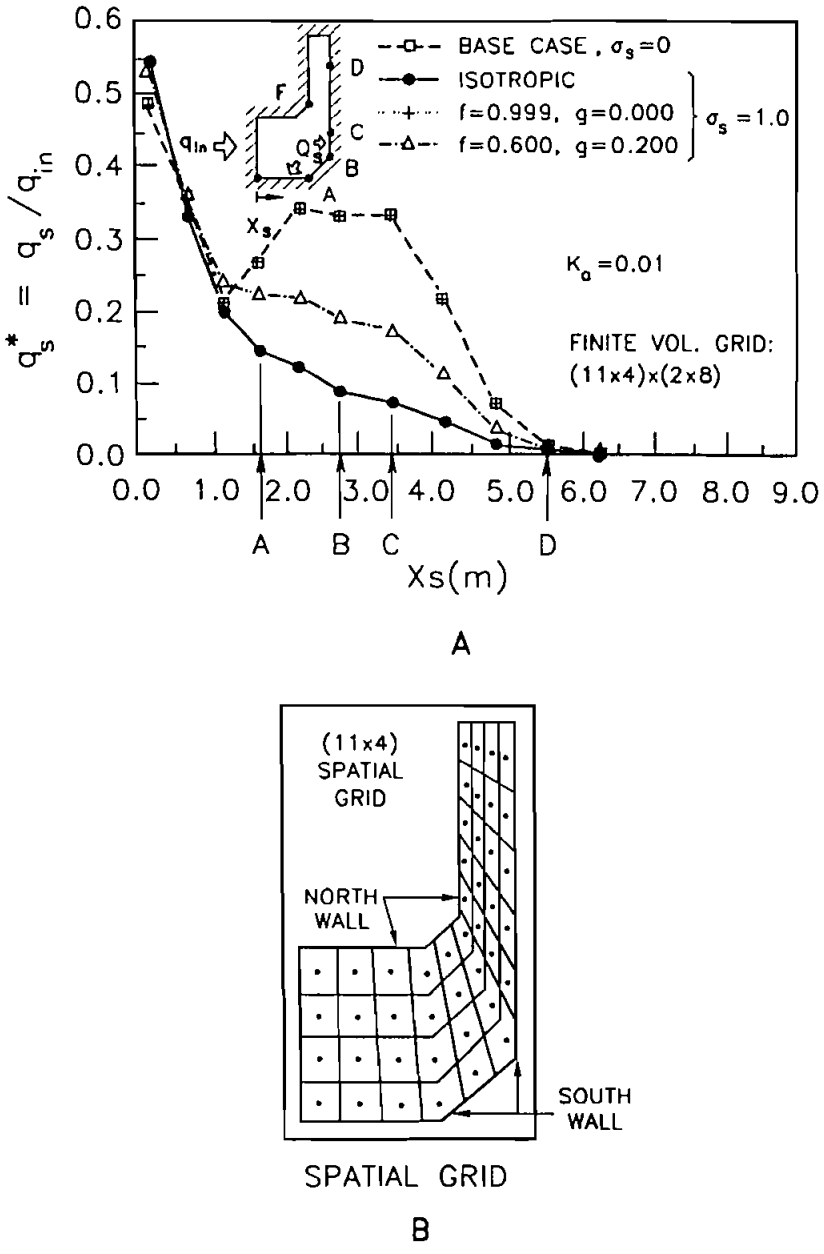

Fig. 9 (A) Nondimensional radiant heat transfer on the south wall of the J-shaped enclosure with a diffuse radiant flux q_{in} incident on the west wall for a medium with $K_a = 0.01$ 1/m and various scattering conditions. f and g refer to nonisotropic scattering parameters [see Eq. (15)]. (B) Control volumes defined by the spatial grid.

Downloaded by [North Carolina State University] at 13:35 08 October 2012

ing, while g is the asymmetry factor. The objective of this test is to predict the net radiant flux to the north and the south walls, defined in Fig. 9B.

Since an exact benchmark solution is not available for this problem, physical arguments will be used to check the reasonableness of the predictions. A relatively coarse grid, $(N_x \times N_y) \times (N_\theta \times N_\phi) = (11 \times 4) \times (2 \times 8)$, is selected for this problem (see Fig. 9B). The net nondimensional radiant flux distribution along the south wall of the channel, $q_s^* = q_s/q_{in}$, is plotted in Fig. 9A for four different scattering conditions. The base case, shown as squares in Fig. 9A, has no scattering at all ($\sigma_s = 0$).

Generally, q_s^* decreases with X_s because radiation is attenuated by absorption and scattering. When scattering is absent, the radiant flux impinging on the wall is very sensitive to its orientation with respect to the source. Thus, q_s^* of the base case (shown as squares) increases from point A because the south wall lies in a more direct line of sight from the source. This increase levels off when it is balanced by the loss due to absorption. Beyond point C, q_s^* drops because the south wall becomes increasingly sheltered from the source, and at point D, the source is completely hidden and q_s^* is correctly predicted to approach zero.

The presence of scattering makes the dependence on wall orientation to the source less crucial. This is especially the case when scattering is isotropic. As a result, q_s^* in this case (shown as filled-in circles in Fig. 9A) diminishes monotonically from $X_s = 0$ to point D without any sudden increase at point A.

However, when scattering is strongly forward ($f \to 1$), the q_s^* distribution (plotted as "+" in Fig. 9A) closely resembles the base case. This result is intuitively correct, because if inscattering and outscattering can occur only in the forward direction, the result should be the same as if no scattering occurred at all.

For the case with $f = 0.6$, $g = 0.2$ (shown as triangles in Fig. 9A), scattering occurs with a moderate preference in the forward direction. The q_s^* direction is expected to lie between the case with almost total forward scattering ($f = 0.999$) and the isotropic scattering case. This expectation is also confirmed in Fig. 9A.

Similar observations can be made regarding the net dimensionless radiant flux distributions along the north wall, $q_n^* = q_n/q_{in}$ (not shown here; see [16]). The prediction correctly shows that q_n^* in the nonscattering case approaches zero beyond point F because the north wall is not directly visible to the source. But when scattering is admitted, the prediction indicates that q_n^* beyond F is nonzero, which is reasonable because scattering spreads some of the radiation to regions beyond point F.

The above test problem requires an iterative process to obtain a converged solution. Typically, 12 cycles of updates are needed to attain a radiant flux value that varies less than 0.01% between cycles. The CPU expense is about 60 s in a VAX 11-785 machine.

SUMMARY

The present article shows how the finite-volume method can be applied on a mesh that consists of nonorthogonal quadrilateral elements. This application encountered only minor obstacles. One obstacle was that, in a general geometry, the boundaries of the discrete solid angles can no longer be chosen to fall along physical boundaries. A simple solution to this problem was proposed. The other obstacle was that, although the equa-

Downloaded by [North Carolina State University] at 13:35 08 October 2012

tions can still be solved most efficiently by sweeping from node to node in a specified order, this order is not obvious for a nonorthogonal mesh. The solution was to develop an algorithm that generates, as part of preprocessing activities, a map of the optimal order.

The method was then applied to three benchmark problems, and one more complex problem where the main check was intuitively correct behavior. Rapid and accurate predictions were found to the benchmark problems, and entirely reasonable behavior was found for the complex problem. It seems that the finite-volume method can now be confidently applied on the same grids that are used to simulate other processes.

Downloaded by [North Carolina State University] at 13:35 08 October 2012

REFERENCES

1. J. R. Howell, Thermal Radiation in Participating Media: The Past, the Present, and Some Possible Futures, *J. Heat Transfer*, vol. 110, pp. 1220–1226, 1988.
2. R. Viskanta and M. P. Mungüç, Radiation Heat Transfer in Combustion Systems, *Prog. Energy Combust. Sci.*, vol. 13, no. 2, pp. 97–160, 1987.
3. M. P. Mengüç and R. Viskanta, Radiative Transfer in Three-Dimensional Rectangular Enclosures Containing Inhomogeneous, Anisotropically Scattering Media, *J. Quant. Spectrosc. Radiat. Transfer*, vol. 33, pp. 533–549, 1985.
4. M. P. Mengüç and R. Viskanta, Radiative Transfer in Axisymmetric, Finite Cylindrical Enclosures, *J. Heat Transfer*, vol. 108, pp. 271–276, 1986.
5. W. A. Fiveland, Three-Dimensional Radiative Heat Transfer Solutions by the Discrete-Ordinates Method, *AIAA J. Thermophys.*, vol. 2, pp. 309–316, 1988.
6. M. E. Larsen and J. R. Howell, The Exchange Factor Method: An Alternative Basis for Zonal Analysis of Radiating Enclosures, *J. Heat Transfer*, vol. 107, pp. 936–942, 1985.
7. R. G. Siddall and N. Selçuk, Evaluation of a New Six-Flux Model for Radiative Transfer in Rectangular Enclosures, *Trans. Inst. Chem. Eng.*, vol. 57, pp. 163–168, 1979.
8. F. C. Lockwood and N. G. Shah, A New Radiation Solution Method for Incorporation in General Combustion Prediction Procedures, *18th Symp. (Int.) on Combustion*, The Combustion Institute, pp. 1405–1414, 1981.
9. G. D. Raithby and E. H. Chui, A Finite-Volume Method for Predicting Radiant Heat Transfer in Enclosures with Participating Media, *J. Heat Transfer*, vol. 112, pp. 415–423, 1990.
10. E. H. Chui, G. D. Raithby and P. M. J. Hughes, Prediction of Radiative Transfer in Cylindrical Enclosures by the Finite Volume Method, *AIAA J. Thermophys.*, vol. 6, no. 4, pp. 605–611, 1992.
11. E. H. Chui and G. D. Raithby, An Implicit Solution Scheme to Improve Convergence Rate in Radiative Transfer Problems, *Numer. Heat Transfer*, vol. 22, no. 3, pp. 251–272, 1992.
12. R. Siegel and J. R. Howell, *Thermal Radiation Heat Transfer*, 2d ed., McGraw-Hill, New York, London, p. 453, 1981.
13. B. R. Baliga and S. V. Patankar, A Control Volume Finite Element Method for Two-Dimensional Fluid Flow and Heat Transfer, *Numer. Heat Transfer*, vol. 6, pp. 245–261, 1983.
14. G. E. Schneider and M. J. Raw, Control Volume Finite-Element Method for Heat Transfer and Fluid Flow Using Colocated Variables. 1. Computational Procedure, *Numer. Heat Transfer*, vol. 11, pp. 363–390, 1987.
15. S. S. Dua and P. Cheng, Multi-Dimensional Radiative Transfer in Non-isothermal Cylindrical Media with Non-isothermal Bounding Walls, *Int. J. Heat Mass Transfer*, vol. 18, pp. 245–259, 1975.
16. E. H. Chui, Modelling of Radiative Heat Transfer in Participating Media by the Finite Vol-

ume Method, Ph.D. thesis, Department of Mechanical Engineering, University of Waterloo, Waterloo, Ontario, Canada, 1990.
17. J. H. Joseph and W. J. Wiscombe, The Delta-Eddington Approximation for Radiative Heat Transfer, *J. Atmos. Sci.*, vol. 33, pp. 2452-2459, 1976.

Received 10 February 1992
Accepted 24 April 1992

Downloaded by [North Carolina State University] at 13:35 08 October 2012